Research Article Vol. 33, No. 19 / 22 Sep 2025 / Optics Express 41423

Optics EXPRESS

Stable non-volatile phase modulation with antimony-based phase shifter on a broadband silicon nitride platform

AFROOZ SHOAA,[1,*] QIANBIN LUO,[1] THALIA DOMINGUEZ BUCIO,[1] MEHDI BANAKAR,[1] ISAAC JOHNSON,[1] ELLIOT SANDELL,[1] JOAQUIN FANECA,[2] IOANNIS ZEIMPEKIS,[1,3] AND FREDERIC GARDES[1]

[1] *Optoelectronics Research Centre, University of Southampton, Southampton SO17 1BJ, UK*
[2] *Microelectronics Institute of Barcelona, IMB-CNM (CSIC), 08193 Barcelona, Spain*
[3] *Electronics and Computer Science, University of Southampton, Southampton SO17 1BJ, UK*
[*] *as1v20@soton.ac.uk*

Abstract: Silicon-based photonics is a leading platform for scalable and low-power photonic integrated circuits (PICs). However, conventional modulation methods suffer from high power consumption and volatility, particularly when using the silicon nitride platform. Phase change materials (PCMs) provide a compelling alternative, enabling nonvolatile and low-loss switching with a high refractive index contrast (Δn). In this work, we demonstrate, for the first time to the best of our knowledge, the integration of an n-doped polysilicon microheater to induce phase transitions in antimony selenide (Sb_2Se_3) on a silicon nitride (SiN_x) platform in the C-band. The device utilizes controlled electrical pulses to achieve a phase shift of 0.43π by switching Sb_2Se_3 between its amorphous and crystalline states over 7900 cycles, with an extinction ratio of up to 12.5 dB and a variation of ±1.9 dB over the entire 7900 cycles. These results highlight the potential scalability of this approach for broadband photonic switching applications that require nonvolatile functionality.

1. Introduction

Pioneered by Soref and Petermann in the late 1980s and early 1990s, silicon photonics laid the foundation for integrated optics in silicon, enabling PICs to guide and manipulate light on a single chip while overcoming traditional electronic interconnection limitations such as transmission speed and high power consumption [1]. However, conventional light modulation mechanisms, such as thermo-optic [2,3] and free-carrier effects [4] suffer from limitations in refractive index modulation ($\Delta n < 0.01$), and therefore, typically require a long interaction length to achieve a π-phase shift, often exceeding 100 µm ($L_\pi > 100$ µm), leading to large device footprints. Moreover, the thermo-optic effect in silicon nitride platforms operating in the C-band can cause thermal crosstalk between closely spaced components, where heat from one element affects neighboring devices, resulting in parasitic phase shifts. This often necessitates complex control circuitry to manage these effects [5,6]. Additionally, achieving effective modulation requires high static power consumption due to the inherently low thermo-optic coefficient ($\Delta n \sim 2.5 \times 10^{-5}\,K^{-1}$) of silicon nitride [7].

To overcome these limitations of volatile tuning mechanisms in silicon photonics, chalcogenide PCMs offer a promising alternative for programmable PICs [8,9]. PCMs can switch reversibly between two distinct structural states, amorphous and crystalline, resulting in significant refractive

#575054 https://doi.org/10.1364/OE.575054
Journal © 2025 Received 1 Aug 2025; revised 10 Sep 2025; accepted 11 Sep 2025; published 19 Sep 2025

index changes that surpass those achieved with traditional methods [10–12]. Crucially, this phase transition is nonvolatile, maintaining the state without requiring constant power input [12–15].

These combined properties, along with their compatibility with existing silicon photonics fabrication processes, position PCMs as ideal candidates for compact, energy-efficient, and highly flexible PICs. In modern PCM-based modulators, thermal switching via external microheaters has emerged as a superior technique for inducing phase transitions with high contrast and efficiency [16–21].

Integrated microheaters, including materials and structures like PIN diodes [14,20,22], uniformly doped silicon [10,23,24], graphene [25], indium tin oxide (ITO) [18,26], and fluorine-doped tin oxide (FTO) [27] utilize Joule heating through precisely controlled electrical pulses to induce phase transitions in PCMs. This method outperforms direct free-space heating of PCMs with focused far-field laser pulses, which requires precise alignment and poses challenges for scalability in large-scale photonic integration [21]. Alternatively, on-chip direct heating of PCMs using near-field light pulses eliminates the need for external alignment. However, this approach faces challenges in switching large PCM areas and less absorptive PCMs, leading to lower switching contrast. Moreover, it increases the complexity of photonic routing and the overall system design [20,28].

Silicon's CMOS compatibility and high thermal conductivity at telecommunication wavelengths make silicon-on-insulator (SOI) the preferred photonic integrated platform for most PCM-based phase modulation experiments that use external heaters to change the PCM's state [13,16,17,19–24,26,28]. However, this material exhibits strong absorption in the visible and short-wavelength near-infrared (<1100 nm), limiting its utility in these ranges [29]. In these wavelength ranges, silicon nitride has become a widely adopted platform for light propagation due to its inherent low optical losses [30]. Other key advantages of silicon nitride over silicon are manufacturing flexibility, the possibility of processing at a lower temperature, refractive index tunability, a higher tolerance to phase error, and reduced sensitivity to thermal fluctuations [5].

Emerging low-loss PCMs, such as Sb_2Se_3 [10,22], antimony sulphide (Sb_2S_3) [31], and germanium antimony selenide telluride (GSST) [32], have attracted significant attention as alternatives to the widely used germanium antimony telluride (GST), which exhibits high optical losses, particularly in its crystalline state [33,34]. Among these low-loss PCMs, Sb_2Se_3 and Sb_2S_3 offer wider band gaps and extremely small extinction coefficients ($k < 10^{-4}$) at 1310 nm and 1550 nm in both amorphous and crystalline states, whereas GSST exhibits a higher extinction coefficient in the crystalline state ($k \approx 0.42$), leading to comparatively larger optical losses despite remaining low-loss in its amorphous state [35].

In [13], the first investigation into the low optical loss and phase modulation properties of Sb_2S_3 on a silicon nitride platform at 750 nm wavelength highlighted its potential as a broadband PCM in the near-infrared region. Furthermore, Sb_2S_3 and Sb_2Se_3 were later integrated with Mach-Zehnder interferometer (MZI) building blocks on a SiN_x platform, showcasing the advantages of this platform when combined with these PCMs in the O- and C-bands compared to SOI technology [36]. The effective refractive index changes (Δn_{eff}) for Sb_2S_3 were measured to be 0.05 at 1310 nm and 0.02 at 1550 nm, while Sb_2Se_3 exhibited a change of 0.03 at 1310 nm and 0.05 at 1550 nm. Despite the promising low-loss properties and phase modulation capabilities of Sb_2Se_3 and Sb_2S_3, the previous studies [13,36] have not investigated their thermoelectrical cyclability when integrated with a SiN_x platform, particularly using integrated microheaters.

Here, for the first time, we demonstrate the integration of an n-doped polysilicon external microheater to induce phase transitions in Sb_2Se_3 on a SiN_x platform in the C-band. This novel configuration enables stable and efficient switching, requiring 19.2 µJ for crystallization and 0.54 µJ for amorphization. The device exhibits enduring operation over 7900 switching cycles through controlled electrical pulses (13 V for crystallization and 30 V for amorphization), with an average extinction ratio of 12.4 dB maintained throughout. These results highlight the device's robustness and effectiveness in nonvolatile optical switching, marking a significant step toward nonvolatile and reconfigurable photonic devices leveraging PCMs on SiN_x platforms.

2. Methods

2.1. Device fabrication

The process involved creating passive components on a 400 nm-thick, low-pressure chemical vapor deposited (LPCVD) silicon nitride layer using precise lithographic and etching techniques. This LPCVD SiNx layer was deposited on a 3.2 µm-thick thermally oxidized silicon dioxide (SiO_2) layer grown on an 8-inch silicon substrate. After patterning, the resist features were inspected with critical dimension scanning electron microscopy (CD-SEM) to confirm accurate pattern transfer and dimensional compliance. Next, the SiNx layer was etched using inductively coupled plasma (ICP) dry etching for precise anisotropic etching of the passive device structures. To produce a clean surface, residual photoresist was removed via plasma cleaning with a dielectric asher.

Subsequently, wafer surfaces underwent RCA cleaning to eliminate organic and inorganic contaminants, preparing the SiNx surface for further processing. A 2 µm-thick oxide layer was deposited using plasma-enhanced chemical vapor deposition (PECVD), followed by a three-step chemical mechanical planarization (CMP) process to effectively embed the SiNx core within the oxide. An 80 nm n-doped polysilicon layer was then deposited on the SiNx optical devices with PECVD, patterned through DUV lithography. The pattern was etched with ICP, and residual resist was removed with plasma cleaning. The wafer was again cleaned with RCA. To prevent dopant outgassing during doping activation via rapid thermal annealing (RTA), a 20 nm PECVD oxide layer was deposited beforehand.

The RTA was conducted at 1050°C for 60 seconds. Afterward, a 20 nm intrinsic polysilicon layer was deposited by PECVD to taper the PCM layer, reducing mode mismatch and enhancing coupling efficiency. DUV lithography was then used to pattern the wafer's photoresist, followed by ICP etching to define the intrinsic polysilicon layer. Metal contact formation began with DUV lithography to pattern the contact regions. Reactive ion etching (RIE) was used to selectively remove silicon and silicon dioxide to create contact openings, with profilometer checks verifying etch depth accuracy throughout.

A hydrofluoric acid (HF) wet etch removed native oxide from these openings. Subsequently, a physical vapor deposition (PVD) process sputtered Ti/Al/Ti metal stack into the patterned contacts. Multiple lift-off steps, involving solvent washes like edge bead remover (EBR), acetone, and isopropyl alcohol (IPA), ensured metal remained only in designated areas, removing residual metal and photoresist. An oxygen (O_2) RIE descum finalized the contact patterning.

The PCM pattern was transferred via DUV lithography onto the wafer, then etched with RIE to form the PCM structures. The PCM material was deposited by PVD, using an AJA sputtering system. To prevent oxidation and thermal reflow of the Sb_2Se_3 layer, a 40 nm SiO_2 encapsulation was applied. The lift-off process involved multiple solvent washes, including acetone, IPA, and EBR, to remove unwanted resist and define the PCM regions precisely. Finally, wafer dicing separated individual dies, completing the fabrication process and preparing them for testing and characterization. Throughout the process, film characterization was conducted after each deposition and etching step using spectroscopic ellipsometry.

2.2. Experimental setup

A tuneable laser source (Agilent 81940A) operating within the 1520–1630 nm wavelength range was employed to provide the optical input to the DUT. A polarization controller was used to adjust the polarization state of the light to the TE mode. The DUT was mounted on a three-dimensional stage for precise alignment. A Panasonic camera (CAM 06) was employed to monitor the alignment process visually. An Edmund optics fiber illuminator provided adequate lighting to enhance visibility. For inducing phase transitions in the PCM, two pulse profiles, one for amorphization and another for crystallization, were generated by a pulse generator (BNC model 577). A controlled time delay between the two channels ensured a non-overlapping sequence, with the two pulse trains combined via a 2:1 combiner (API 1515) to produce a single, continuous output. The combined signal was then directed to the metal contacts of the phase shifter.

The use of two separate channels for pulse generation was necessary due to the limitations of the pulse generator, which did not allow for amplitude modification on a single channel. Once the pulses were applied to the DUT, the transmitted light was directed to a power meter (Keysight 81634B) for optical power measurement. Simultaneously, the optical output was monitored and recorded in real-time on an oscilloscope (RSDS 1204CFL). This enabled the capture of changes in optical power corresponding to the phase transitions within the PCM.

To precisely quantify the set and reset energies delivered to the DUT, the BNC model 577 pulse generator was used to apply switching pulses, while the DUT response was simultaneously monitored using the RSDS 1204CFL oscilloscope operating with two channels. Channel 1, configured with a 1 MΩ input impedance, measured the total voltage V_{total} across the DUT and the 50 Ω internal termination of channel 2. Channel 2, set to a 50 Ω input impedance, measured the voltage drop across its internal termination resistor, which was connected in series with the DUT and thus acted as a calibrated current-sensing element. The instantaneous current through the DUT was determined from the channel 2 signal using Ohm's law, $I = \frac{V_{CH2}}{50\Omega}$. The corresponding voltage across the DUT was then calculated by subtracting the small voltage drop across the termination resistor from the total voltage as $V_{DUT} = V_{total} - (I \times 50\Omega)$. From these quantities, the instantaneous power dissipated in the DUT was obtained as $P = V_{DUT} \times I$.

Finally, the total switching energy was evaluated by multiplying the average power by the pulse duration, with 300 µs pulses applied for set operations and 1.5 µs pulses for reset operations.

3. Results

This work's PCM-based optical phase shifter (OPS) operates through Joule heating generated by an integrated microheater. As shown in Fig. 1(a), to induce crystallization, a low-amplitude, long-duration 'SET' pulse (13 V, 300 µs) is applied to heat the PCM above its crystallization temperature (Tc = 200 °C). This thermal process promotes atomic rearrangement, causing the transition to the crystalline phase with a higher refractive index [40]. Conversely, for amorphization, a high amplitude 'RESET' pulse (30 V) of much shorter duration (1.5 µs) is used to heat the PCM above its melting point (Tm = 620 °C). Rapid cooling, achieved by quickly removing the excitation, quenches the material and transforms it into an amorphous state with a lower refractive index [20].

The optical optimization of the device was performed employing the eigenmode expansion (EME) method in ANSYS Lumerical, focusing on a 400 nm-thick, 1 µm-wide SiN_x strip waveguide designed for single-mode transverse electric (TE) operation. A polysilicon microheater was designed above this SiN_x waveguide and beneath the integrated Sb_2Se_3 layer. The analysis revealed a noticeable mode mismatch between the bare SiN_x waveguide and the OPS, with an 85% overlap between their supported modes, indicating a considerable coupling loss at the interface. To mitigate this mode mismatch, symmetric polysilicon tapers were introduced on both sides of the PCM layer. These tapers gradually adjust the mode profile, enabling near-adiabatic optical field coupling between the SiN_x waveguide and the OPS region. Thus, they minimize scattering and reflection losses, enhancing mode conversion efficiency.

As depicted in Fig. 1(b), a comprehensive three-step simulation workflow was carried out using ANSYS Lumerical to optimize the taper layout profile for efficient optical coupling. In the first step, finite-difference time-domain (FDTD) simulations were employed to assess the effect of the taper's outer tip width on insertion loss. As shown in Fig. 1(c), the results indicate

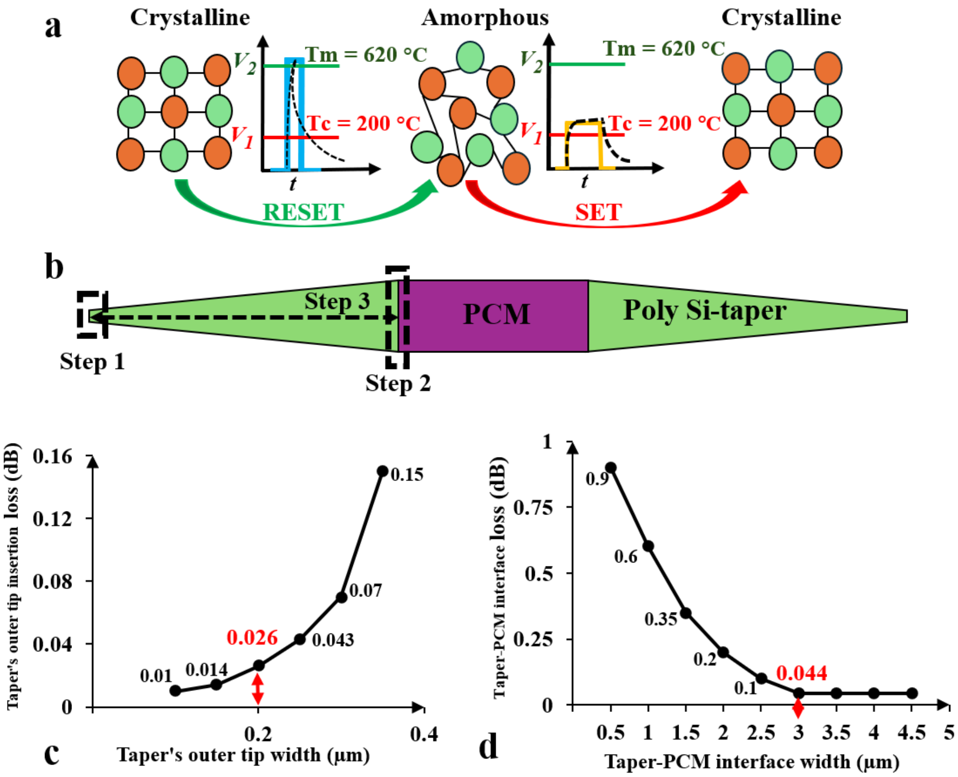

Fig. 1. (a) Thermoelectrical switching mechanism in a PCM-based phase modulator, where controlled electrical pulses induce crystallization (SET) and amorphization (RESET), resulting in refractive index changes. (b) Three-step simulation process for optimizing the top-down view of the tapers on both sides of the PCM layer. (c) FDTD analysis of the polysilicon taper's outer tip width and its impact on insertion loss. A minimum feature size of 200 nm was selected as the optimal outer tip width, corresponding to an insertion loss of 0.026 dB. (d) Demonstration of interface loss as a function of the taper-PCM interface width. The insertion loss decreases with increasing interface width and saturates at ~0.044 dB for widths greater than or equal to 3 µm; therefore, this value (3 µm) was selected as the optimal design parameter.

that increasing the taper's outer tip width leads to higher insertion loss. Given the fabrication constraints of the 248 nm deep ultraviolet (DUV) lithography equipment used throughout the fabrication process, which imposed a minimum feature size of 200 nm, this value was selected for the taper's outer tip. Using this dimension, the simulated insertion loss stands at 0.026 dB, as highlighted in Fig. 1(c).

In the second step, FDTD analysis was used to evaluate the impact of the taper-PCM interface width on insertion loss. As shown in Fig. 1(d), the insertion loss decreases with increasing taper-PCM interface width, eventually stabilizing at 0.044 dB when the width reaches 3 µm or more. Based on this behaviour, a 3 µm taper-PCM interface width was selected to ensure optimal performance while minimizing insertion loss. For the final step, EME analysis was conducted to optimize the overall taper length. The simulation results indicated that a taper length of 35 µm allows for an adiabatic mode transition, leading to efficient optical coupling. Specifically, the transmission at this length was nearly 100%, signifying minimal coupling loss. Considering the losses from the taper's outer tip and the taper-PCM interface, the total predicted loss for the two 35 μm tapers was calculated to be 0.14 dB.

To determine the required PCM length for achieving a π-phase shift, Eq. (1) was employed [37]. This equation relates the phase shift ($\Delta\phi$) to the Δn_{eff} between the two PCM states through the operating wavelength (λ), and the propagation length (L) over which the phase shift occurs. In this case, the propagation length corresponds to the PCM length.

$$\Delta\phi = \frac{2\pi}{\lambda} \cdot \Delta n_{\mathrm{eff}} \cdot L \tag{1}$$

To achieve a π-phase shift, $\Delta\phi$ was set to be π in Eq. (1), leading to Eq. (2) for propagation length (L) measurement:

$$L = \frac{\pi.\lambda}{2\pi.\Delta n_{\mathrm{eff}}} = \frac{\lambda}{2.\Delta n_{\mathrm{eff}}} \tag{2}$$

To compute L using Eq. (2), the Δn_{eff} was first determined. This value was obtained through finite-difference eigenmode (FDE) simulations conducted in ANSYS Lumerical, utilizing optical property data for Sb_2Se_3 in both its amorphous and crystalline states at a wavelength of 1550 nm, as investigated and reported in [38]. The simulated structure comprised a 20 nm-thick Sb_2Se_3 layer deposited on an 80 nm polysilicon microheater integrated atop a SiN_x waveguide. The thickness of 20 nm for Sb_2Se_3 was selected as it facilitates significant optical modulation while maintaining minimal insertion loss, as demonstrated by prior work [39]. The simulations yielded effective refractive indices of 2.17 and 2.21 for the amorphous and crystalline states, respectively, resulting in Δn_{eff} of 0.04.

Substituting this value and an operating wavelength of 1.55 μm into Eq. (2), the required PCM length to obtain a π-phase shift is around 20 μm. The schematic of the PCM-based optical phase shifter unit, incorporating a 20 nm-thick Sb_2Se_3 cell, is shown in Fig. 2(a). This 20 μm-long, and 3 μm-wide Sb_2Se_3 cell is integrated atop an 80 nm phosphorus-doped polysilicon microheater, positioned on a 400 nm thick,1 μm wide SiN_x strip waveguide.

To induce phase transition, electrical pulses were delivered to the phase shifter via metal contacts composed of a thin titanium (Ti) adhesion layer, followed by aluminum (Al) for conductivity, and a final thin Ti layer. Figure 2(b) presents a micrograph of asymmetrical MZIs featuring integrated optical phase shifter units in both arms and a zoom-in of one of the phase shifter units.

The passive experimental characterization of bare MZI began with the measurement of its insertion loss. To isolate the intrinsic loss of the MZI itself, this measurement was normalized to remove the coupling losses associated with the grating couplers and fiber interfaces, as well as the propagation loss of the straight SiN_x waveguide segment. After normalization, the insertion loss of the bare MZI was measured to be less than 3 dB.

This remaining loss is primarily attributed to excess losses in the multimode interferometers (MMIs) and bend-induced losses within the interferometer arms.

To experimentally determine the propagation loss associated with the OPS, a cutback method was employed next [40]. This unit was integrated into straight waveguides with the OPS lengths ranging from 20 to 80 μm, in 20 μm increments, as illustrated in Fig. 3(a). The measured losses for both amorphous and crystalline states are plotted in Fig. 3(b) as a function of the OPS length.

The linear fits to the data demonstrate propagation losses of 0.13 dB/μm for the amorphous state and 0.15 dB/μm for the crystalline state, indicating that the crystalline phase exhibits slightly higher loss. Before initiating phase transition with electrical pulses, a DC experiment was performed to determine the voltage at which a noticeable nonvolatile shift in the MZI's transmission spectrum occurs.

This shift, observed at 10.5 V, indicates the threshold voltage for the amorphous to crystalline transition of the 20 μm-long PCM. This value served as an approximate lower limit for the voltage

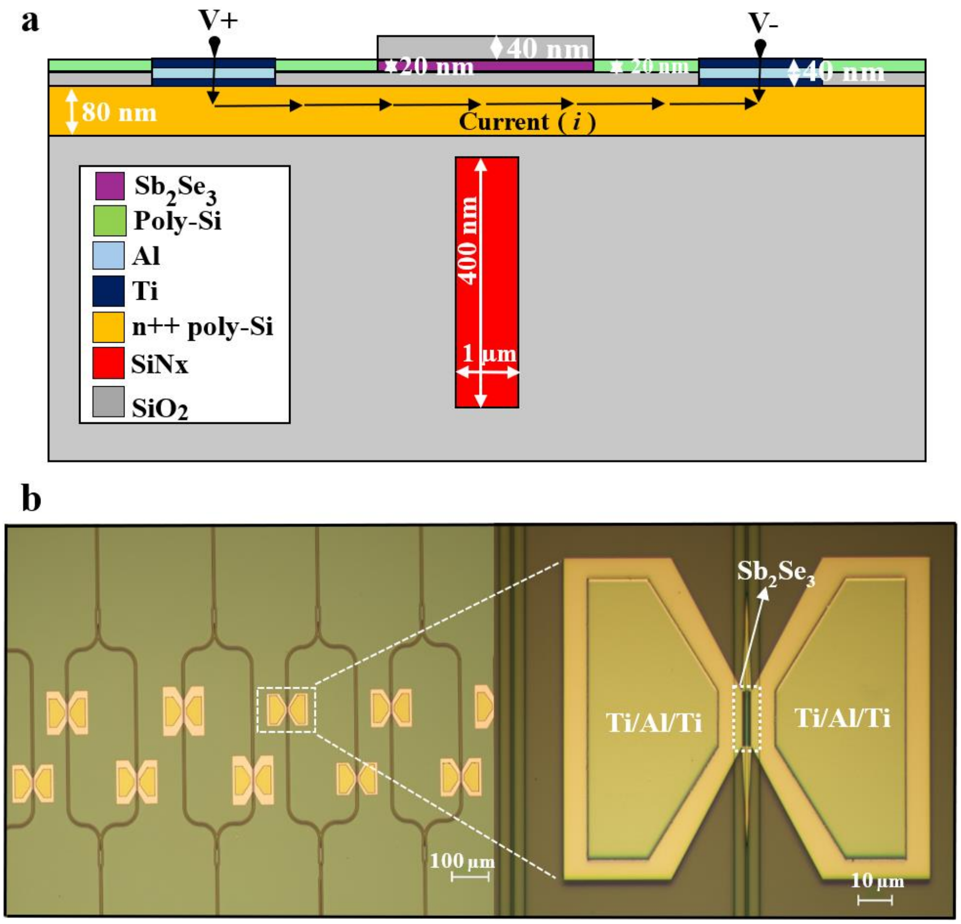

Fig. 2. (a) The schematic representation of the PCM-based phase shifter unit, featuring a 20 nm thick Sb_2Se_3 cell on an 80 nm thick phosphorus-doped polysilicon microheater, integrated with a 400 nm thick SiN_x waveguide optimized for TE mode operation. (b) A micrograph of asymmetrical MZIs with the integrated optical phase shifters in both arms, accompanied by a high-magnification view of a phase shifter unit highlighting its key structural components.

required to initiate crystallization using electrical pulses. Subsequently, multiple trials with varying pulse profiles were conducted to determine the optimal configuration, which consisted of a set pulse of 13 V with a duration of 300 µs. This profile results in an energy consumption of 19.2 µJ and effectively balances energy efficiency with the desired shift in the transmission spectrum.

To achieve a 0.43π-phase shift, a 30 V reset pulse with a duration of 1.5 µs was applied to the OPS unit, which consists of a 20 nm thick, 20 µm-long, and 3 µm-wide Sb_2Se_3 cell. This pulse raised the temperature above the PCM's melting point to induce amorphization, corresponding to an energy consumption of 0.54 µJ. The minimum achievable reset pulse width was constrained by the voltage limitation of the driver used in the experimental setup, detailed in the "Methods- Experimental Setup". When operating two channels simultaneously, the pulse generator's maximum output is capped at 30 V. This voltage ceiling restricts the amount of energy delivered during shorter pulse durations, thereby preventing the OPS from reaching the energy density necessary to trigger the phase transition. Figure 3(c) demonstrates that the MZI's

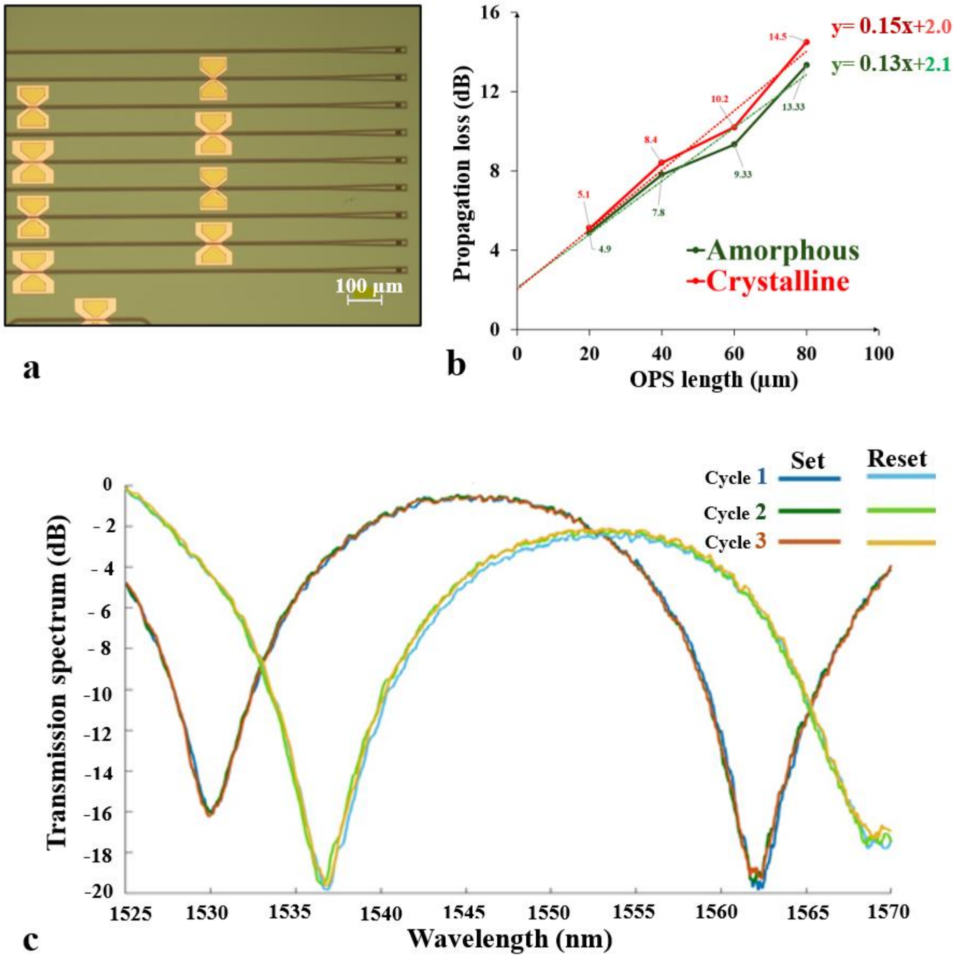

Fig. 3. (a) Fabricated phase shifter units on straight waveguides with varying OPS lengths. (b) Measured propagation loss for both amorphous and crystalline PCM states via the cutback method application. (c) Demonstration of the transmission spectrum of the device over three-phase transition cycles, highlighting repeatable optical modulation.

transmission spectrum undergoes a phase transition from an amorphous to a crystalline state over three cycles. The spectral shift observed indicates a phase shift in the device induced by the nonvolatile change in the PCM's state and optical properties.

Using the experimental setup described in the "Methods- Experimental Setup " section, we further evaluated the switching units' state retention and cycling stability within the MZIs by applying an overall 15800 set and reset pulses while recording the resulting temporal trace shown in Fig. 4(a).

The phase shifter exhibited reliable and reversible switching transitions over 7900 cycles, maintaining an acceptable overall mean extinction ratio of 12.4 dB. Over the first 4150 cycles, the extinction ratio averaged 14 dB, representing a deviation of +1.6 dB from the overall mean. In the subsequent cycles, the extinction ratio averaged 10.5 dB, producing a deviation of -1.9 dB from the overall mean. This resulted in a maximum variation of ±1.9 dB, underscoring the device's consistent performance and robustness over prolonged cycling. Figure 4(b) illustrates this trend, highlighting the device's stability and endurance over 7900 switching events.

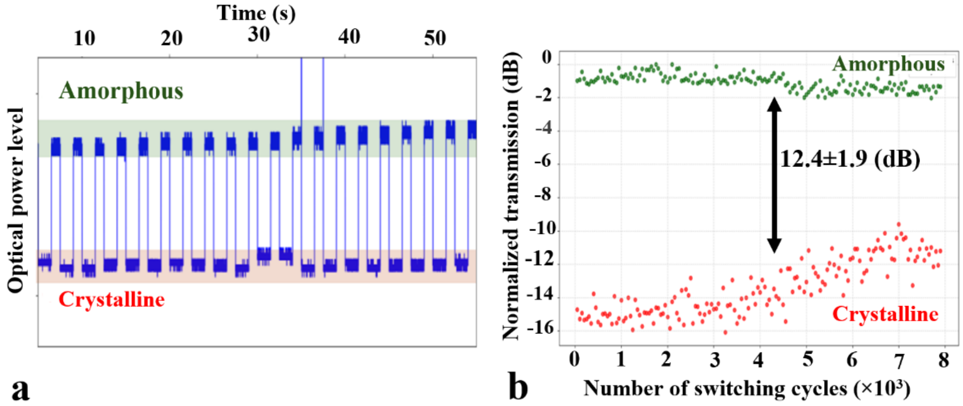

Fig. 4. (a) Temporal response of the device under test (DUT) subjected to set and reset pulses, showing distinct optical power levels corresponding to phase transitions. (b) Cyclability demonstration of the switching unit over 7,900 cycles, showing stable performance with an average extinction ratio value of 12.4 dB and a variation of ±1.9 dB. The transmission is normalized to the transmission of a bare waveguide. The data has been smoothed using a 50-point moving average to clearly show the trends in the extinction ratio.

4. Discussion

We have demonstrated the electrothermal tuning of an Sb_2Se_3-based OPS on a SiN_x platform operating within the C-band. Sb_2Se_3 was selected over Sb_2S_3 because, while both materials exhibit similarly low extinction coefficients of $k < 10^{-4}$ in the C-band for both states, Sb_2Se_3 offers a higher refractive index contrast between its amorphous and crystalline states, approximately 0.17 greater than Δn of Sb_2S_3 [38]. N-doped polysilicon serves as the microheater material due to its CMOS compatibility and ease of integration with existing waveguide systems [41].

To assess the endurance of our device, we conducted 7900 switching cycles and obtained a stable mean extinction ratio of 12.4 dB, with an average of 14 dB and a peak of 15.2 dB during the initial 4150 cycles. Simultaneously, we monitored the microheater's reliability through current-voltage (I-V) measurements. As depicted in Fig. 5, the microheater's resistance remained within ∼1.2% of its initial value for the first 4150 cycles. However, it then gradually increased to ∼2.6% at 7900 cycles. After 7950 cycles, however, the resistance abruptly rose by ~67%, signaling the microheater failure. This sudden degradation directly corresponded to a sharp drop in extinction ratio, which limited the device's operational life to 7900 cycles. We therefore identify the microheater's degradation as the primary limiting factor for device endurance, and further optimisation of the microheater could improve endurance. This conclusion is supported by the normalised transmission data shown in Fig. 4(b) in the "Result" section. The crystalline-state transmission in Fig. 4(b) shows a gradual increase over the first 7,900 cycles, closely following the slow rise in heater resistance, before degrading more sharply after heater failure. This strong correlation indicates that the performance of the microheater directly affects the Δn_{eff} and extinction ratio. The apparent variations in refractive indices, specifically in crystalline states, as well as the decline in extinction ratio, can therefore be explained by the same mechanism: once the microheater degradation sets in, the increased resistance and reduced heating uniformity lead to incomplete phase transitions, thereby lowering the refractive index contrast.

While the microheater's degradation clearly dominates the device lifetime, the PCM itself can also contribute. Over extended cycling, Sb_2Se_3, particularly in its crystalline state, may undergo gradual optical drift due to cycling-induced material fatigue, a phenomenon well-documented in PCMs and typically associated with oxidation and atomic rearrangements [42–46].

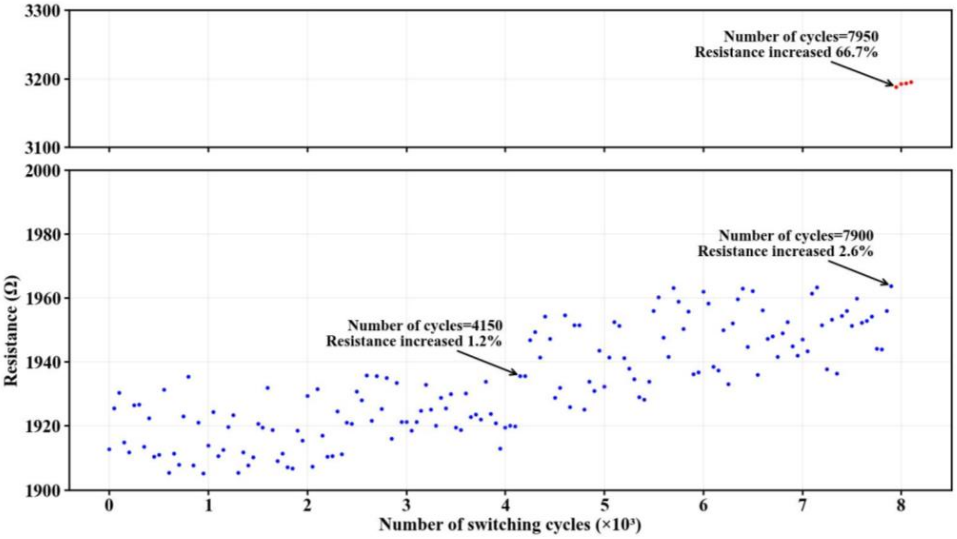

Fig. 5. Demonstration of the microheater's electrical resistance as a function of the number of switching cycles. The resistance remains stable for the first ~7900 cycles before a sharp increase indicates failure of the microheater.

However, the close correlation between the increase in the microheater's resistance and the corresponding degradation in the optical response (Figs. 5 and 4(b)) indicates that PCM-related fatigue plays a subordinate role under the present conditions. Nevertheless, improved encapsulation strategies could mitigate oxidation and stabilize PCM properties, potentially extending overall endurance [47].

The high set and reset peak voltages employed in the experiments further highlight the need for optimization of the microheater. Elevated switching voltages are symptomatic of resistive losses in the doped polysilicon microheater. Optimizing doping concentration and annealing conditions could improve conductivity and reduce the required voltage for switching the PCM.

Alternative transparent, low-loss materials such as graphene [25], ITO [18,26], and FTO [27] have been proposed as microheaters in PCM-based devices. These materials could reduce resistive losses, expand the transparency window, and improve heating efficiency. However, such materials are not fully CMOS compatible, and further studies are needed to evaluate their integration, reversible switching behavior, and long-term stability on $\mathrm{SiN_X}$ photonic platforms.

In addition to the endurance evaluation, the phase-shift analysis provides valuable insight into the factors shaping overall device performance. While the experimentally observed $\Delta\phi$ was limited to 0.43π, approximately half of the initially predicted value of a π-phase shift for a 20 μm-long PCM segment within the configuration.

This deviation is primarily attributed to a lower actual change in the Δn_{eff} than assumed in the initial simulations. The original estimate of $\Delta\phi$ was based on a simulated Δn_{eff} of 0.04, assuming a Δn of about 0.7 between the amorphous and crystalline states of the PCM. This assumption aligns with a prior study involving full crystallization from the as-deposited amorphous phase via hot-plate annealing [38]. However, such conditions differ markedly from those in our study, where phase transitions are driven electrically. In this context, amorphization is typically partial, and PCM's optical properties can deviate from those of the as-deposited state.

Consequently, both Δn and the corresponding Δn_{eff} are likely lower than the values used in the initial model, leading to lower $\Delta\phi$. Employing Eq. (3), we experimentally extracted Δn_{eff} of 0.017, about half of the initial simulated Δn_{eff} of 0.04 [38], underscoring the limitations of relying on as-deposited material parameters for accurate device-level predictions.

$$\Delta n_{eff} = \frac{\lambda}{L} \times \frac{\Delta\lambda}{FSR} \tag{3}$$

In Eq. (3), λrepresents the operating wavelength (1.55 μm), L is the length of the PCM (20 μm), FSR is the experimentally measured free spectral range, and $\Delta\lambda$ is the wavelength shift observed in the transmission spectrum throughout the cycling process.

To further investigate this discrepancy, a simulation-based approach utilizing Lumerical eigenmode analysis was employed to determine the actual Δn based on the empirically derived Δn_{eff}. Instead of assuming a fixed Δn of ~ 0.7, which corresponds to a complete and uniform phase transition via hot plate annealing [38], the Δn was systematically varied in the simulations until the computed Δn_{eff} closely matched the experimentally observed value of 0.017, ultimately revealing a Δn of about 0.3, further supporting the conclusion that the phase transition during thermoelectrical cycling is partial. Furthermore, the heat gradient in the microheater, arising from its structural design, leads to localized heating and inefficient optical phase modulation. This effect is potentially driven by a thermal runaway phenomenon, in which the central region of the heater experiences elevated temperatures, further reducing its resistance and drawing more current, thereby reinforcing the temperature imbalance [10].

Consequently, PCM undergoes a non-uniform phase transition, which diminishes Δn_{eff} and thereby limits the maximum achievable phase shift. This thermal non-uniformity is demonstrated through COMSOL Multiphysics simulations under the application of a 30 V amorphization pulse to the OPS for a duration of 1.5 μs. Figure 6(a) presents the simulated temperature distribution along the PCM segment, spanning from −10 μm to +10 μm relative to the device center. The figure demonstrates a pronounced peak within the central region, specifically between −5 μm and +5 μm. This localized heating results from current crowding, which drives a thermal runaway effect that further amplifies the central temperature rise [10]. In addition, Fig. 6(b) shows a top-down, color-mapped thermal profile of the device, clearly illustrating spatial temperature variations and inconsistent thermal distribution along the PCM layer.

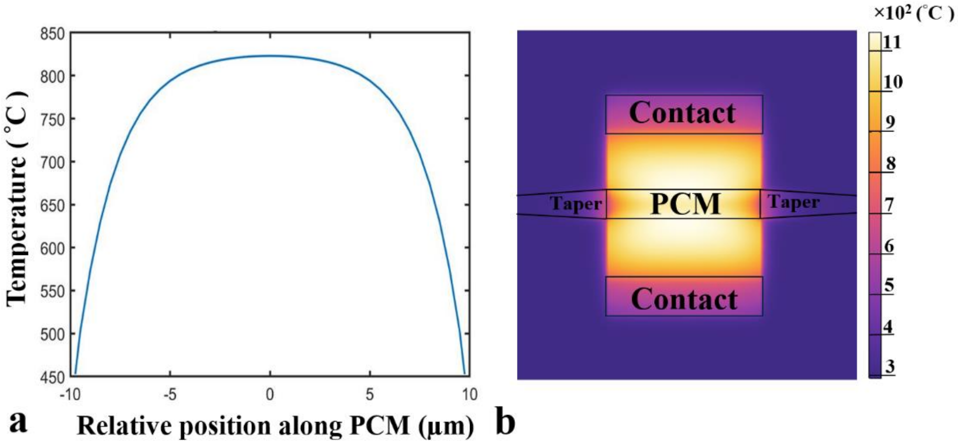

Fig. 6. (a) Simulated temperature distribution along the PCM layer, plotted from −10 μm to +10 μm relative to the center of the device, during a 30 V, 1.5 μs amorphization pulse. (b) Top-down COMSOL simulation of the temperature profile under the same pulse conditions, indicating spatial thermal non-uniformity across the PCM layer.

In summary, while our CMOS-compatible Sb_2Se_3-based OPS on SiN_x demonstrates strong potential for nonvolatile active light modulation, key challenges remain. Endurance testing revealed a strong correlation between microheater resistance and optical response, establishing microheater degradation as the primary lifetime-limiting factor. The elevated set and reset voltages delivered to DUT further underscore the need for the microheater's optimization. Phase-shift measurements confirm partial phase transitions and non-uniform thermal distributions within the microheater, both of which restrict modulation efficiency. These limitations may be addressed through improved microheater design, optimized doping and annealing strategies, and the exploration of alternative materials offering higher conductivity, better transparency, and compatibility with the SiN_x platform. Overcoming these challenges is key to realizing energy-efficient, high-performance nonvolatile broadband photonic devices that fully leverage the advantages of SiN_X integration for broader application reach.

Funding. European Union's Horizon 2020 Research and Innovation Programme (PlasmoniAC 871391, OCTAPUS 101070009); Horizon Europe – Work Programme 2021-2022 research and innovation programme (AMBROSIA 101093166); Engineering and Physical Sciences Research Council (EPSRC) studentship (EP/W022931/1); Ministerio de Ciencia y Innovación (MCIN) / Agencia Estatal de Investigación (AEI); European Union "NextGenerationEU/PRTR" (RYC2023-043256-I, FJC2020-042823-I).

Acknowledgment. This research was conducted at the Optoelectronics Research Centre, Faculty of Engineering and Physical Sciences, University of Southampton. The authors gratefully acknowledge the support, facilities, and infrastructure provided by the University of Southampton.

Disclosures. The authors declare that they have no conflict of interest.

Data availability. The data for this work is accessible at [48].

References

1. B. Schuppert, J. Schmidtchen, and K. Petermann, "Optical channel waveguides in silicon diffused from GeSi alloy," Electron. Lett. **25**(22), 1500–1502 (1989).
2. D. Pérez, I. Gasulla, L. Crudgington, *et al.*, "Multipurpose silicon photonics signal processor core," Nat. Commun. **8**(1), 636 (2017).
3. F. Gao, W. Xie, J. Y. Tan, *et al.*, "Comprehensive investigation of thermo-optic phase shifters on a multi-layered SiN-on-SOI platform," J. Lightwave Technol. **41**(10), 3108–3114 (2023).
4. G. Reed, D. Thomson, W. Zhang, *et al.*, *Optical modulators in integrated photonics for data communication applications* (Elsevier, 2023), pp. 69–121.
5. T. D. Bucio, C. Lacava, M. Clementi, *et al.*, "Silicon nitride photonics for the near-infrared," IEEE J. Sel. Top. Quantum Electron. **26**(2), 1–13 (2020).
6. D. Pérez, J. Fernández, R. Baños, *et al.*, "Switching and cross-talk characteristics of compact thermal tuners on a silicon nitride platform," in *18th European Conference on Integrated Optics* (2016).
7. R. Pradip, V.S.A. Varri, L. McRae, *et al.*, "Fast thermo-optic switching on silicon nitride platform through parity-time symmetry breaking," arXiv (2024).
8. S. Abdollahramezani, O. Hemmatyar, H. Taghinejad, *et al.*, "Tunable nanophotonics enabled by chalcogenide phase-change materials," Nanophotonics **9**(5), 1189–1241 (2020).
9. Z. Fang, R. Chen, J. Zheng, *et al.*, "Non-volatile reconfigurable silicon photonics based on phase-change materials," IEEE J. Sel. Top. Quantum Electron. **28**(3), 8200317 (2022).
10. C. Ríos, Q. Du, Y. Zhang, *et al.*, "Ultra-compact nonvolatile phase shifter based on electrically reprogrammable transparent phase change materials," PhotoniX **3**(1), 26 (2022).
11. J. Zheng, A. Khanolkar, P. Xu, *et al.*, "GST-on-silicon hybrid nanophotonic integrated circuits: a non-volatile quasi-continuously reprogrammable platform," Opt. Mater. Express **8**(6), 1551–1561 (2018).
12. P. Xu, J. Zheng, J. K. Doylend, *et al.*, "Low-loss and broadband nonvolatile phase-change directional coupler switches," Acs Photonics **6**(2), 553–557 (2019).
13. Z. Fang, J. Zheng, A. Saxena, *et al.*, "Non-volatile reconfigurable integrated photonics enabled by broadband low-loss phase change material," Adv. Opt. Mater. **9**(9), 2002049 (2021).
14. R. Chen, Z. Fang, J. E. Froch, *et al.*, "Broadband nonvolatile electrically controlled programmable units in silicon photonics," ACS Photonics **9**(6), 2142–2150 (2022).
15. Z. Fang, R. Chen, J. Zheng, *et al.*, "Ultra-low-energy programmable non-volatile silicon photonics based on phase-change materials with graphene heaters," Nat. Nanotechnol. **17**(8), 842–848 (2022).
16. Y. Zhang, J. B. Chou, J. Li, *et al.*, "Broadband transparent optical phase change materials for high-performance nonvolatile photonics," Nat. Commun. **10**(1), 4279 (2019).
17. N. Farmakidis, N. Youngblood, X. Li, *et al.*, "Plasmonic nanogap enhanced phase-change devices with dual electrical-optical functionality," Sci. Adv. **5**(11), eaaw2687 (2019).
18. H. Zhang, L. Zhou, L. Lu, *et al.*, "Miniature multilevel optical memristive switch using phase change material," ACS Photonics **6**(9), 2205–2212 (2019).

19. Y. Lu, M. Stegmaier, P. Nukala, *et al.*, “Mixed-mode operation of hybrid phase-change nanophotonic circuits,” Nano Lett. **17**(1), 150–155 (2017).
20. J. Zheng, Z. Fang, C. Wu, *et al.*, “Nonvolatile electrically reconfigurable integrated photonic switch enabled by a silicon PIN diode heater,” Adv. Mater. **32**(31), 2001218 (2020).
21. Z. Fang, *Non-volatile programmable photonics based on phase-change materials* (University of Washington, 2023).
22. X. Yang, L. Lu, Y. Li, *et al.*, “Non-Volatile Optical Switch Element Enabled by Low-Loss Phase Change Material,” Adv. Funct. Mater. **33**(42), 2304601 (2023).
23. J. Zheng, Z. Fang, C. Wu, *et al.*, *Nonvolatile Electrically Reconfigurable Integrated Photonic Switch Enabled by an In-Situ Silicon PIN Heater*.
24. D. Wu, X. Yang, N. Wang, *et al.*, “Resonant multilevel optical switching with phase change material GST,” Nanophotonics **11**(15), 3437–3446 (2022).
25. C. Ríos, Y. Zhang, M. Y. Shalaginov, *et al.*, “Multi-level electro-thermal switching of optical phase-change materials using graphene,” Adv. Photonics Res. **2**(1), 2000034 (2021).
26. K. Kato, M. Kuwahara, H. Kawashima, *et al.*, “Current-driven phase-change optical gate switch using indium–tin-oxide heater,” Appl. Phys. Express **10**(7), 072201 (2017).
27. N. Youngblood, C. Talagrand, B. F. Porter, *et al.*, “Reconfigurable low-emissivity optical coating using ultrathin phase change materials,” ACS Photonics **9**(1), 90–100 (2022).
28. J. Zheng, S. Zhu, P. Xu, *et al.*, “Modeling electrical switching of nonvolatile phase-change integrated nanophotonic structures with graphene heaters,” ACS Appl. Mater. Interfaces **12**(19), 21827–21836 (2020).
29. J. Faneca, S. Garcia-Cuevas Carrillo, E. Gemo, *et al.*, “Performance characteristics of phase-change integrated silicon nitride photonic devices in the O and C telecommunications bands,” Opt. Mater. Express **10**(8), 1778–1791 (2020).
30. M. Blasco-Solvas, B. Fernández-Vior, J. Sabek, *et al.*, “Silicon Nitride Building Blocks in the Visible Range of the Spectrum,” J. Lightwave Technol. **42**(17), 6019–6027 (2024).
31. R. Chen, Z. Fang, C. Perez, *et al.*, “Non-volatile electrically programmable integrated photonics with a 5-bit operation,” Nat. Commun. **14**(1), 3465 (2023).
32. Q. Zhang, Y. Zhang, J. Li, *et al.*, “Broadband nonvolatile photonic switching based on optical phase change materials: beyond the classical figure-of-merit,” Opt. Lett. **43**(1), 94–97 (2018).
33. C. Ríos, M. Stegmaier, P. Hosseini, *et al.*, “Integrated all-photonic non-volatile multi-level memory,” Nat. Photonics **9**(11), 725–732 (2015).
34. H. Zhang, L. Zhou, B. Rahman, *et al.*, “Ultracompact Si-GST hybrid waveguides for nonvolatile light wave manipulation,” IEEE Photonics J. **10**(1), 2200110 (2018).
35. Y. Xu, S. Liu, T. Liu, *et al.*, “Optical switch based on Ge2Sb2Se4Te1-assisted racetrack microring,” in *Photonics* (MDPI, 2022).
36. J. Faneca, I. Zeimpekis, S. T. Ilie, *et al.*, “Towards low loss non-volatile phase change materials in mid index waveguides,” Neuromorph. Comput. Eng. **1**(1), 014004 (2021).
37. B.E. Saleh and M.C. Teich, *Fundamentals of photonics* (John Wiley & Sons, 2019).
38. M. Delaney, I. Zeimpekis, D. Lawson, *et al.*, “A new family of ultralow loss reversible phase-change materials for photonic integrated circuits: Sb2S3 and Sb2Se3,” Adv. Funct. Mater. **30**(36), 2002447 (2020).
39. S. Blundell, T. W. Radford, I. A. Ajia, *et al.*, “Ultracompact programmable silicon photonics using layers of low-loss phase-change material Sb2Se3 of increasing thickness,” ACS photonics **12**(3), 1382–1391 (2025).
40. C. H. Levine, “More on cutback management: Hard questions for hard times,” Public administration review **39**(2), 179–183 (1979).
41. R. M. Krishna, A. Eftekhar, S. Lee, *et al.*, “Polysilicon micro-heaters for resonance tuning in CMOS photonics,” Opt. Lett. **47**(5), 1097–1100 (2022).
42. M. Wuttig and N. Yamada, “Phase-change materials for rewriteable data storage,” Nat. Mater. **6**(11), 824–832 (2007).
43. S. Raoux, W. Wełnic, and D. Ielmini, “Phase change materials and their application to nonvolatile memories,” Chem. Rev. **110**(1), 240–267 (2010).
44. W. Zhang, R. Mazzarello, M. Wuttig, *et al.*, “Designing crystallization in phase-change materials for universal memory and neuro-inspired computing,” Nat. Rev. Mater. **4**(3), 150–168 (2019).
45. M. Lee, R. Cheek, C. Chen, *et al.*, “The impact of hole-induced electromigration on the cycling endurance of phase change memory,” in *International Electron Devices Meeting* (IEEE, 2010).
46. S. Lee, J. H. Jeong, T. S. Lee, *et al.*, “A study on the failure mechanism of a phase-change memory in write/erase cycling,” IEEE Electron Device Lett. **30**(5), 448–450 (2009).
47. C. Shi, M. Xu, X. Guo, *et al.*, “Characteristics, encapsulation strategies, and applications of Al and its alloy phase change materials for thermal energy storage: a comprehensive review,” Adv. Funct. Mater. **35**(2), 2412914 (2025).
48. A. Shoaa, “Dataset supporting the paper "Stable non-volatile phase modulation with antimony-based phase shifter on broadband silicon nitride platform",” University of Southampton Institutional Research Repository (2025), https://doi.org/10.5258/SOTON/D3606.